Dynamic individual pitch control for wake mitigation
Why does the helix handedness in the wake matter?

Coquelet, M.; Gutknecht, J.; Van Wingerden, J. W.; Duponcheel, M.; Chatelain, P.

DOI
10.1088/1742-6596/2767/9/092084

Publication date
2024

Document Version
Final published version

Published in
Journal of Physics: Conference Series

Dynamic individual pitch control for wake mitigation: Why does the helix handedness in the wake matter?

Journal of Physics: Conference Series **2767** (2024) 092084 doi:10.1088/1742-6596/2767/9/092084

Dynamic individual pitch control for wake mitigation: Why does the helix handedness in the wake matter?

M Coquelet[1], J Gutknecht[1], JW van Wingerden[1], M Duponcheel[2], P Chatelain[2]

[1] Delft Center for Systems and Control, Delft University of Technology, The Netherlands.
[2] Institute of Mechanics, Materials and Civil Engineering, UCLouvain, Belgium.

E-mail: m.coquelet@tudelft.nl

Abstract. Wind farm flow control aims at mitigating wake effects in order to maximize power production in wind farms. This work mostly focuses on the Helix strategy, which relies on individual pitch control to radially offset the application point of the thrust force from the rotor center and to dynamically change its azimuthal position. Previous studies have shown that power gains for a downstream turbine are higher for a counter-clockwise (CCW) rotation of the application point than for a clockwise (CW) one. In the CCW case, the wake develops as a right-handed helix, while in the CW case, a left-handed helix is observed. Using Large Eddy Simulations, this paper shows that the helix handedness in the wake matters due to its interaction with the wake swirl. Results of the CCW and CW helix first highlight the formation of streamwise vorticity in the near wake, which is transformed into strong coherent vortices in the far wake. Those vortex structures, to some extent similar to the counter-rotating vortex pair in the wake of yawed wind turbines, are responsible for (i) displacing the wake thanks to their induced velocities and (ii) deforming the shape of the wake.

1. Introduction

As wind flows through a wind turbine, a wake characterized by slow velocity and high turbulence is formed, leading to power losses in wind farm configurations. In the quest for a more efficient production of wind-sourced energy, finding strategies to mitigate wakes is essential [1].

Static flow control strategies have originally been investigated, including wake steering ones [2]. Yaw misalignment has repeatedly shown positive results in terms of power gains and is now commercialized by some wind turbine manufacturers [3]. The power gains associated to this technique are the result of the wake being steered away from the downstream turbines. Indeed, the thrust force exerted on a yawed rotor comprises a component acting perpendicularly to the mean flow field, which forces the lateral displacement of the wake. Bastankhah and Porté-Agel [4] showed that this transverse force is responsible for the formation of a pair of counter-rotating vortices in the wake. Their presence implies that, as the wake propagates downstream, it is deformed and takes a so-called kidney shape [4]. Fleming et al. [2] investigated whether wake redirection could be reproduced by keeping the rotor aligned but rather inducing an asymmetric distribution of the out-of-plane forces over the rotor using individual pitch control (IPC). Results show that such a method only resulted in a marginal wake deflection. IPC can indeed offset the resultant thrust from the rotor center, hence generating a (yaw) moment on the rotor. Yet this does not lead to the lateral displacement of the wake, as there is no lateral force (see Fig. 1(b)).

More recently, the dynamic version of these wake redirection techniques has been investigated. Dynamic yaw control was presented in Munters and Meyers [5], with dynamic changes of rotor yaw misalignment. The application of such a strategy is currently limited by yaw actuators, whose responsiveness is still too slow for the time scales at stake. The dynamic counterpart of the aforementioned IPC strategy is the so-called helix control [6]. As suggested earlier, IPC can be used to generate an uneven distribution of out-of-plane forces on the rotor, i.e. to displace the application point of the resultant thrust force from the rotor center. While this offset of the application point was kept static in Fleming et al. [2], it rotates around the rotor center with the helix control. The rotation can either be clockwise (CW), i.e. in the same direction as the rotor rotation, or counter-clockwise (CCW). It has been shown both numerically [6, 7, 8, 9] and experimentally [10] that dynamic IPC does result in the lateral displacement of the wake. The latter appears in a rotating manner, leading to the wake propagating as a left-handed or right-handed helix, for CCW and CW helix control respectively (see Fig. 1(c,d)). Several studies have shown that the CCW helix was more beneficial than the CW one in terms of power gains for a downstream turbine. This suggests that the direction of rotation of the helix forcing interacts with the direction of rotation of the rotor and possibly with the wake swirl. An argument in this favor is provided in the work of de Vos et al. [11], where the helix is mimicked in a wind tunnel using a porous disc. As the turbine is modeled as a pure drag device, there is no swirl in the wake. In that case, the CCW helix does not outperform the CW one.

This paper aims at understanding why the helix handedness in the wake matters, i.e. why CCW and CW do not perform equivalently. This question is addressed by investigated the link between the helix rotation and the swirl in the wake. A corollary question to be answered is why dynamics matters for IPC-based wake mitigation strategies, i.e. why a rotating offset of

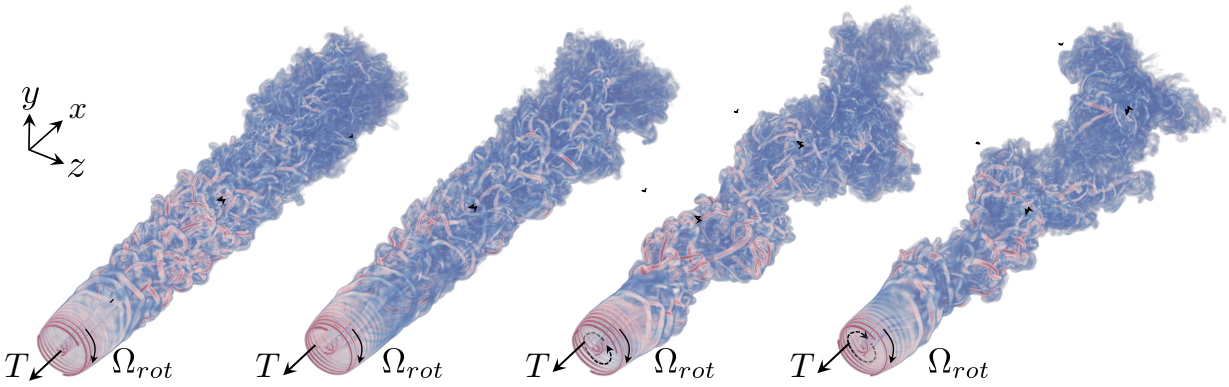

(a) Baseline control (b) Static IPC control (c) CCW helix control (d) CW helix control

Figure 1. Volume rendering of the instantaneous vorticity field of the controlled wakes.

2. Methodology and set-up

The four controllers used in this paper, i.e. baseline (BL), static IPC (ST), CCW helix (CCW) and CW helix (CW), are introduced hereunder along with the LES code used to test them.

2.1. Controllers

The baseline case consists in a state-of-the-art Maximum Power Point Tracking controller [12].

For the IPC controllers, we make use of the Coleman transform to map fixed-frame targets to rotating-frame ones [13]. The individual blade pitch angles $\beta_{1,2,3}$ are retrieved from the

fixed-frame pitch angles, β_{tilt} and β_{yaw}, based on the inverse Coleman transform

$$\begin{bmatrix} \beta_1 \\ \beta_2 \\ \beta_3 \end{bmatrix} = \begin{bmatrix} \cos\theta & \sin\theta \\ \cos\left(\theta - \frac{2\pi}{3}\right) & \sin\left(\theta - \frac{2\pi}{3}\right) \\ \cos\left(\theta + \frac{2\pi}{3}\right) & \sin\left(\theta + \frac{2\pi}{3}\right) \end{bmatrix} \begin{bmatrix} \beta_{\text{tilt}} \\ \beta_{\text{yaw}} \end{bmatrix}, \tag{1}$$

where θ is the azimuthal position of the first blade ($\theta = 0$ when the blade is pointing upward).

The ST controller is implemented so as to statically impose a lateral offset of the thrust force on the turbine, i.e. $\beta_{\text{tilt}} = 0$ and $\beta_{\text{yaw}} = A$, where A is the amplitude of the pitch actuation.

The helix strategy is implemented by imposing sinusoidal variations of the fixed-frame pitch angles, namely $\beta_{\text{tilt}} = A\sin(2\pi f\ t)$ and $\beta_{\text{yaw}} = \pm A\cos(2\pi f\ t)$ (positive for CCW and negative for CW). This will force the rotation of the thrust application point with a frequency f defined by the Strouhal number $St = fD/U_{ref}$, based on the rotor diameter D and the wind speed U_{ref}.

2.2. Numerical solver and set-up

Simulations are performed using a Vortex Particle-Mesh method in which wind turbine blades are represented by Immersed Lifting Lines [14]. The boundary conditions are inflow-outflow in the streamwise direction (x) and unbounded in the transverse directions (y and z). The unbounded conditions imply that the path and direction of the streamlines are not constrained and can connect to the infinite outer domain. This enables the simulation of rotors in tight domains while guaranteeing no blockage effects or forced induction [15]. In this case, the dimensions of the numerical domain are $12D \times 4D \times 4D$.

Simulations of the NREL 5MW immersed in an unsheared 9 m/s inflow are presented. Turbulent fluctuations characterized by an intensity of 1% are added to the inflow in order to prevent numerical effects regarding the triggering of wake recovery. Turbulence is generated by a Mann box [16] whose dimensions are $16D \times 4D \times 4D$. In the context of this study, we avoid higher turbulence as it is known to naturally enhance the meandering of the wake.

Simulations are performed with a $D/h = 64$ resolution, where h is the mesh size and is constant throughout the domain. The size σ of the lifting line mollification kernel is equal to the mesh size, i.e. $\sigma = h = D/64$. Such a combination of grid resolution and force mollification enables the shedding of individual tip vortices, yet those are still too smeared to produce pairing and merging instabilities (see Fig. 1). This partial capture of the near-wake vortex system aligns with numerical studies of dynamic wake control in the literature [6, 7, 9]. In addition, the discussion presented in this paper considers the impact of the helix control on the large-scale structures in the wake. Cheung et. al. [9] recently suggested that the instabilities of these large-scale shear-flow structures are the dominant mechanism explaining the benefits of dynamic flow control strategies, rather then the smaller-scale tip vortex instabilities. The $D/h = 64$ resolution is therefore deemed appropriate for this investigation.

We choose a common value of 0.25 for the Strouhal number [6]. The amplitude of the pitch actuation is chosen to be rather high, $A = 4^{\text{o}}$, in order to exacerbate the effects of the controllers on the wake behavior, as shown in Fig. 1.

3. Results

In this section, we first show how the pitch actuation of the different control strategies translates in terms of forces acting on the rotor. We then discuss how these impact the behavior of the near wake. We further highlight dominant vortex structures developing in the far wake and eventually provide a quantitative analysis of wake displacement and power available in the wake.

3.1. Forces acting on the rotor

This section highlights the effect of the controllers on the forces developing on the rotor. We first define the quantities presented in Fig. 2. Consider the distribution $f_{n,b}(r)$ of the normal force

acting on blade b. Integrating this force along all radial position of the blades r from hub (R_{hub}) to tip (R) and over the three blades provides the rotor thrust force $T = \sum_{b=1}^{3} \left(\int_{r=R_{hub}}^{r=R} f_{n,b}(r) dr \right)$. As discussed in the introduction, the IPC controllers generate an uneven distribution of out-of-plane forces on the rotor, hence shifting the point of application of that thrust force. We further refer to that point as the thrust center (TC) and its coordinates (y_{TC}, z_{TC}) are computed as

$$y_{TC} = \frac{\sum_{b=1}^{3} \left(\int_{r=R_{hub}}^{r=R} f_{n,b}(r) y_b(r) dr \right)}{\sum_{b=1}^{3} \left(\int_{r=R_{hub}}^{r=R} f_{n,b}(r) dr \right)} \quad \text{and} \quad z_{TC} = \frac{\sum_{b=1}^{3} \left(\int_{r=R_{hub}}^{r=R} f_{n,b}(r) z_b(r) dr \right)}{\sum_{b=1}^{3} \left(\int_{r=R_{hub}}^{r=R} f_{n,b}(r) dr \right)}. \tag{2}$$

Now consider the forces acting in the rotor plane. Integrating the distribution $f_{t,b}(r)$ of tangential forces over the three blades provides the resultant in-plane force, which can have a vertical component F_y and a horizontal one F_z.

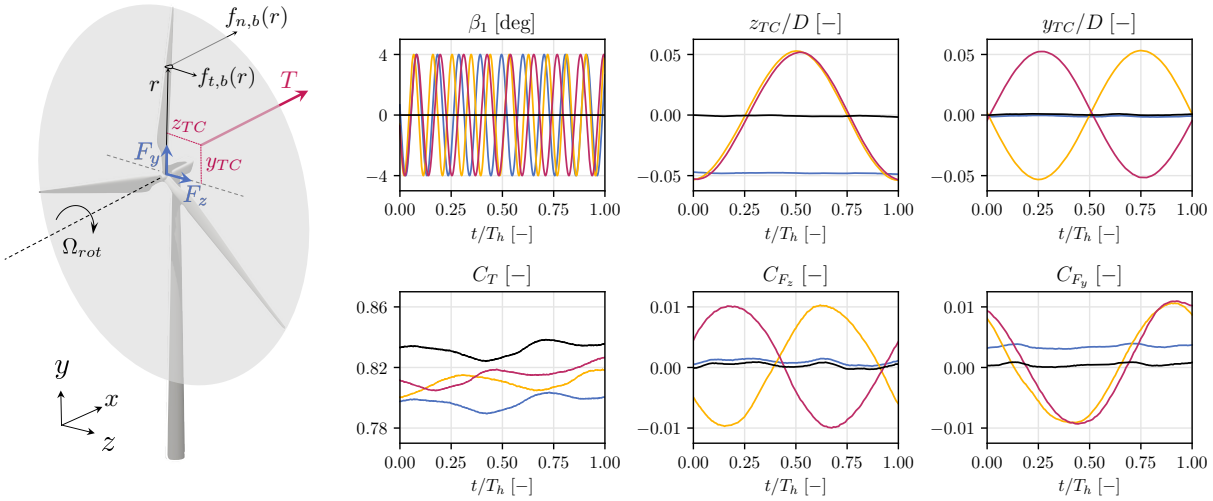

(a) Loads definition. (b) Pitch, thrust coefficient, in-plane forces coefficients, thrust center position.

Figure 2. (a) Schematic representation of resulting in-plane forces ($F_{y,z}$) and out-of-plane force (T). (b) Evolution of pitch angle and forces over one helix period T_h for BL (—), ST (—), CCW (—), CW (—). All force-related signals are notch-filtered at 3P for clarity purposes and forces are made dimensionless following $C_* = */\left(0.5\rho U_{ref}^2 \pi R^2\right)$, $* = T$, F_y or F_z.

Figure 2 shows that the thrust force is reduced by a few percent when the IPC controllers are active, the loss is the biggest for the ST case (-4%). Looking at the position of the thrust center shows that it coincides with the rotor center for the BL case, it is displaced to the left of the rotor for the ST case and it rotates along the rotor center in the CCW and CW direction for CCW and CW helix, respectively. This is what generates the existence of tilting and yawing moments on the rotor. Figure 2 eventually highlights the in-plane forces resulting from the IPC controllers. The in-plane force for the ST case is purely vertical (F_y) as the thrust vector is horizontally displaced. The helix controllers generate periodic in-plane forces. It is known from the conservation of momentum that the flow should be accelerated in the direction of the force. This is why Korb et. al. [7] suggest that the in-plane forces are responsible for the lateral displacement of the wake as it propagates downstream. Nevertheless, the amplitude of the in-plane forces in the helix cases and in the ST case is marginal. The ratio between the force perpendicular to the flow (in-plane) and the one aligned with the flow (thrust) is about 1%. Note that in the case of yaw control, the same forces ratio is given by the sine of the yaw angle.

Considering a yaw angle of 20° for instance, this results in a ratio of 34%. We therefore wonder if the in-plane force can be considered as the sole driving mechanism of the wake displacement.

3.2. Near wake behavior

We first comment the near wake behavior of the BL and ST cases. Figure 3 presents cross-flow slices of the velocity and vorticity flow fields. These are time-averaged ($\overline{*}$ operator) over the extent of the Mann box, i.e. $T_{Mann} = 16D/U_{ref}$. We recall that the vorticity field $\boldsymbol{\omega} = (\omega_x,\ \omega_y,\ \omega_z)$ is defined as the rotational of the velocity field $\boldsymbol{u} = (u_x,\ u_y,\ u_z)$ and reads

$$\boldsymbol{\omega} = \nabla \times \boldsymbol{u} = \left(\frac{\partial u_z}{\partial y} - \frac{\partial u_y}{\partial z}\ ,\quad \frac{\partial u_x}{\partial z} - \frac{\partial u_z}{\partial x}\ ,\quad \frac{\partial u_y}{\partial x} - \frac{\partial u_x}{\partial y} \right). \tag{3}$$

The BL case first shows the axi-symmetry of the velocity deficit (u_x). Secondly, the torque experienced by the blades is responsible for the formation of streamwise vorticity (ω_x), positive at the blade tip and negative at the blade hub. Almost no streamwise vorticity is present in the zone located in between. Thirdly, the signature of the thrust force is the generation of tubes of vorticity tangential to the blade tip and hub, the so-called tip and hub vortices. This tangential vorticity is shown in Fig. 3 through vertical and horizontal vorticity, ω_y and ω_z, as it is projected onto the vertical and horizontal axes, y and z.

In the ST case, one can observe that the wake deficit is not axi-symmetric anymore. This is the result of the IPC actuation, which has shifted the application point of the thrust force to the left of the rotor. The hub and tip vortices are also stronger on the left part of the wake due to the increased loading on that side. They are also more closely spaced due to the reduced convective speed on the left side. These two factors explain why the tip vortices destabilize earlier (from $x/D = 1$ already) on the left side of the wake. What is also remarkable, in comparison with the BL case, is the generation of vertical vorticity ω_y behind the rotor. This is the direct translation, in the vorticity perspective, of the horizontal gradient of streamwise velocity in the inner wake ($\frac{\partial u_x}{\partial z}$ term of ω_y). Another difference with the BL case is the development of two lobes of streamwise vorticity, one positive, one negative, in the inner wake. We explain the appearance of these two lobes based on the vorticity-velocity formulation of the Navier-Stokes equations. These dictate the evolution of vorticity and read

$$\frac{D\boldsymbol{\omega}}{Dt} = (\boldsymbol{\omega} \cdot \nabla)\, \boldsymbol{u} + \nu \nabla^2 \boldsymbol{\omega}\ , \tag{4}$$

where $\frac{D}{Dt} = \frac{\partial}{\partial t} + \boldsymbol{u} \cdot \nabla$ is the Lagrangian derivative and ν is the kinematic viscosity. The left-hand side term represents the advection of vorticity, while the first and second term of the right-hand side correspond to the stretching and the diffusion of vorticity, respectively. The full expression of the streamwise component of the stretching term is

$$(\boldsymbol{\omega} \cdot \nabla)\, \boldsymbol{u}|_x = \omega_x \frac{\partial u_x}{\partial x} + \omega_y \frac{\partial u_x}{\partial y} + \omega_z \frac{\partial u_x}{\partial z} \tag{5}$$

and shows that vertical vorticity ω_y can be stretched into the streamwise direction x under the existence of a vertical gradient of streamwise velocity $\frac{\partial u_x}{\partial y}$. Note that this gradient is not explicitly presented in Fig. 3, yet the horizontal vorticity field $\omega_z = \frac{\partial u_y}{\partial x} - \frac{\partial u_x}{\partial y}$ is a good image of it as the $\frac{\partial u_y}{\partial x}$ term is much smaller than the $\frac{\partial u_x}{\partial y}$ one.

A non-linear effect, vortex stretching, thus explains the formation of a lobe of negative vorticity in the top-left part of the inner wake and of positive vorticity in the lower-left part of the inner wake. One can also observe that the hub vorticity is shifted from the center (black cross) and tends to rotate in the CCW direction. It is carried away by the wake swirl, which

rotates CCW as the rotor rotates CW. Starting from $x/D = 2$, those two lobes are disturbed by the destabilization of the tip vortices on the left-side of the wake and do not persist in the far wake, as Fig. 5 will show.

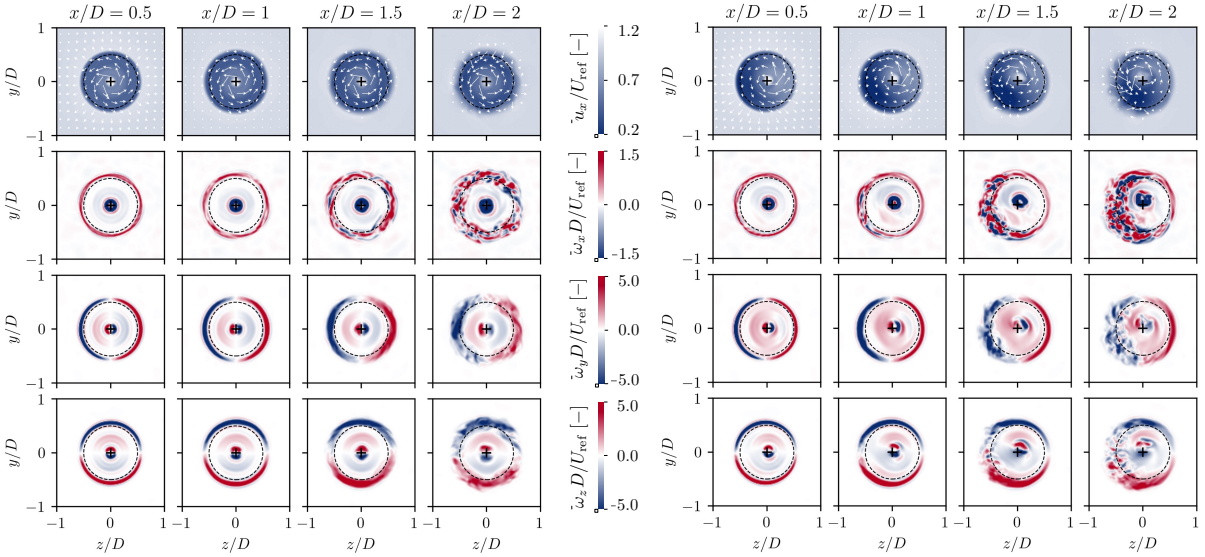

(a) Baseline (b) Static

Figure 3. Time-averaged cross-flow slices of the streamwise velocity field u_x and the three component of the vorticity field, looking from upstream to downstream, at downstream positions ranging from $x/D = 0.5$ to $x/D = 2$. The vector field represents the phase-averaged in-plane velocity component. Circles indicate the rotor position and its center is marked with a cross.

We now transfer the observations made for the ST case to the helix cases. The fields presented in Fig. 4 are phase-averaged, with respect to the phase of the helix control action, over 8 helix periods ($\langle * \rangle$ operator). We highlight how the fluid particles flowing through the rotor at $t/T_h = 0$, i.e. when the rotor loading is similar for CCW, CW and ST, evolve as they are convected downstream. This way, we highlight the differences in the near wake evolution between a static offset of the thrust center, a CCW rotating thrust center and a CW rotating one. To do so, we compute the mean convective speed in the near wake (from $x/D = 0$ to $x/D = 2$) and approximate it to $u_w \simeq 0.5\,U_{\mathrm{ref}}$. The time at which we present the cross-flow slices of the flow fields thus depends on the streamwise position at which the slices are taken, such that

$$\frac{t(x/D)}{T_h} \simeq \frac{x/u_w}{4D/U_{ref}} = \frac{2x/U_{ref}}{4D/U_{ref}} = 0.5\frac{x}{D}. \tag{6}$$

With the CCW helix, the natural swirl of the wake and the rotation of the thrust center are in the same direction. As in the ST case, we see the formation of vertical vorticity ω_y from $x/D = 0.5$, the latter is also stretched into streamwise vorticity ω_x (negative in the top-left quadrant, positive in the bottom-right one). The lobe of positive vorticity tends to spread azimuthally as it is convected downstream and seems to be assimilated with the positive tip vorticity. The lobe of negative vorticity strengthens as the wake develops, but does not merge with the hub vortex. At $x/D = 2$, a vortex system has formed in the wake core and consists of two streamwise negative co-rotating vortices. Such an observation was also recently reported in a communication by Gutknecht et al. [17].

In the CW case, the swirl of the wake and the helix control act in opposite directions. It is remarkable, compared to the CCW case, that the lobe of positive streamwise vorticity created by

stretching is more compact in this case. It is also displaced towards the center of the rotor area (black cross), in the spot originally occupied by the hub vortex which is getting away from it. The hub vortex is also drawn out by the opposite motions of the swirl and the helix control. It spreads azimuthally and ends up merging with the lobe of negative streamwise velocity generated by the stretching. At $x/D = 2$, the streamwise vortex system in the wake core is thus markedly different from that observed in the CCW case. It consists in a positively rotating vortex in the center and a region of negative vorticity, spread over a wide angular extent. This also reminds of the pair of counter-rotating vortices mentioned in Gutknecht et al. [17].

Whether for the CCW or CW case, the vortex systems in the wake core start interacting with the tip vortices from $x/D = 2$. The wake transitions to become turbulent, vortex structures lose their coherence and describing their evolution is more challenging.

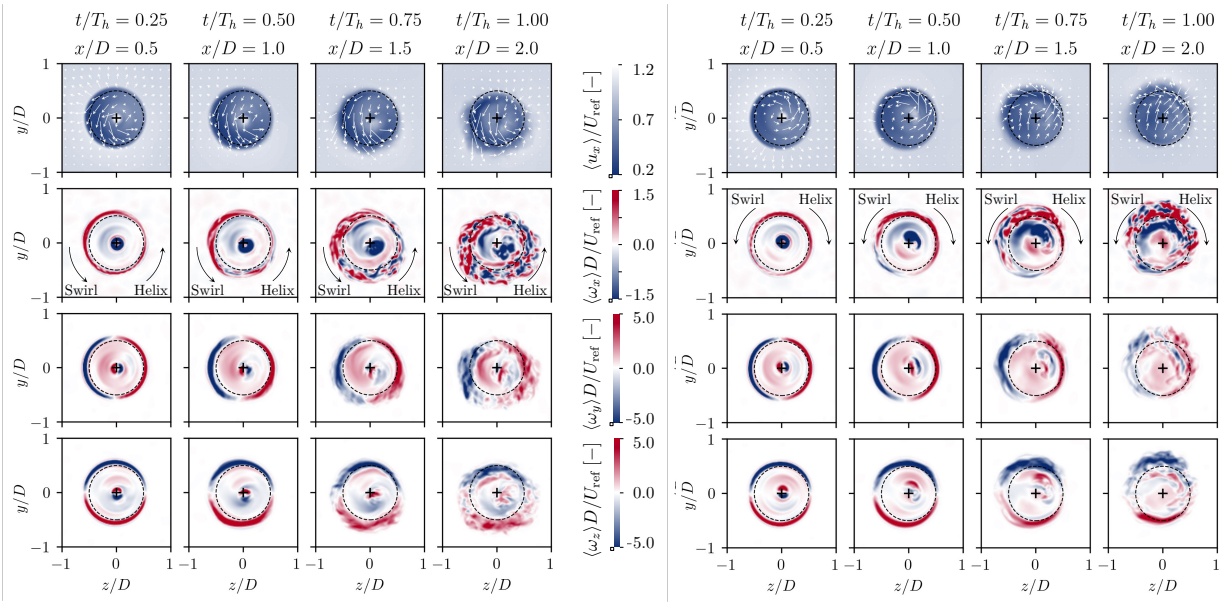

(a) CCW helix

(b) CW helix

Figure 4. Phase-averaged cross-flow slices of the streamwise velocity field u_x and the three component of the vorticity field, looking from upstream to downstream, at downstream positions ranging from $x/D = 0.5$ to $x/D = 2$. The vector field represents the time-averaged in-plane velocity component. Circles indicate the rotor position and its center is marked with a cross.

3.3. Far wake behavior

We now consider the far wake region, where the wake has started to recover and where a downstream turbine would typically be located. Figure 5 shows cross-flow slices of the velocity field at $x/D = 5$ for all four controllers. In the BL case, the wake has propagated as a Gaussian velocity deficit and what remains of the swirl is highlighted by the in-plane velocity field. In the ST case, the signature of the uneven wake deficit is still observable but the wake is not markedly weaker nor displaced from the center position, as it will be quantified in the next section. When it comes to the helix wakes, two specificities appear: (i) the wake is laterally displaced and rotates around the x-axis and (ii) its shape is modified, it is not a Gaussian anymore. The helix wakes are indeed marked by the presence of strong vortex structures, consisting of a two zones of counter-rotating vorticity. This suggests that the vortex systems observed in the near wake have interacted with the tip vortices and formed these new vortex systems in the far wake. In the CCW case, the structure resembles the counter-rotating vortex pair (CVP) that is observed in yawed wakes. The two vortices are located on the contour of the disk region and rotate around

it (dashed-line circle). Note that this was also reported in Korb et al.[7]. In the CW case, the dominant structure within the disk region (dashed-line circle) is the negatively rotating vortex, while a zone of positively rotating vorticity gravitates around it.

The formation of such coherent vortex structures in the wake is beneficial in two ways. First, they help re-injecting high-momentum outer flow within the wake core. Second, the induced velocities they generate cause the wake to displace. Those induced velocities are mostly radial in the CCW case, hence being very efficient in displacing the wake away from a potential downstream rotor (dashed line). In the core of the CW helix, the vortex pair is more asymmetric and the induced velocities tend to be more tangential to the disk area, suggesting reduced benefits for a downstream turbine.

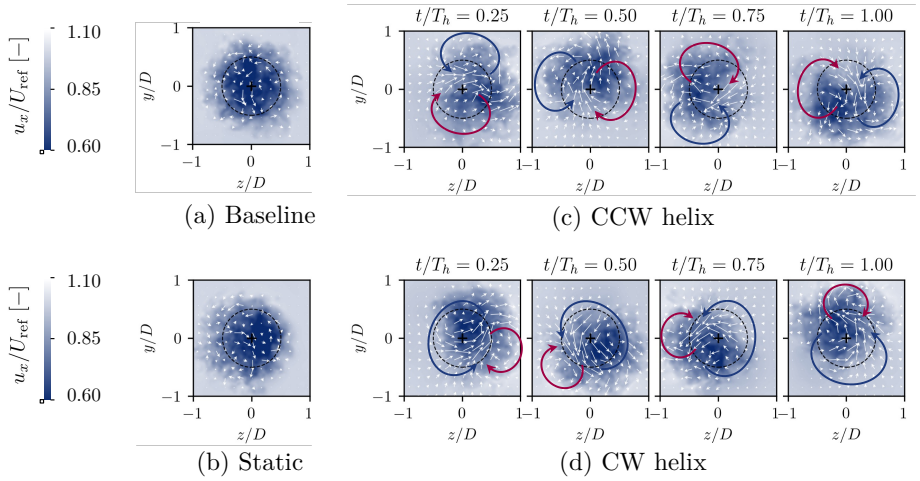

Figure 5. Cross-flow slices of the streamwise velocity field u_x at $x/D = 5$. The vector field represents the in-plane velocity component. Blue and red arched arrows indicate dominant vortex structures in the far wake of the helix. Black circles indicate the rotor position.

3.4. Wake displacement and fraction of available power

We further quantify these two aspects in Fig. 6. We quantify the ability of the vortex system to displace the wake by measuring the position of the wake center. We compute it, following the work of Coudou et. al. [18], as the position (y_{WCL}, z_{WCL}) for which the convolution between the power in the wake and a 2D-Gaussian function is minimum.

The mean distance of the wake center to the x-axis is eventually computed as

$$r_{WCL}(x) = \frac{1}{T_{Mann}} \int_0^{T_{Mann}} \sqrt{(y_{WCL,p}(x,t)^2 + z_{WCL,p}(x,t)^2)}\, dt\ . \tag{7}$$

Figure 6(a) first confirms that the ST controller is not efficient when it comes to wake redirection. In the near wake, one can observe that the WCL is displaced from the center. This is due to the asymmetry of the wake deficit but does not translate, further downstream, into an actual wake displacement, as also reported in [2]. Conversely, it is shown that, with the helix approach, the wake center is significantly displaced as the wake propagates downstream. Also, the displacement is higher with the CCW helix than with the CW one as the wake develops further downstream. This supports the previous discussion on the far wake vortex system.

Finally, we discuss the available power for a turbine that would be located downstream in the wake. We define it as $P_w = \frac{1}{2}\rho\langle u_x^3\rangle_D$, where $\langle * \rangle_D$ indicates the spatial averaging over the disk surface, and normalize it using $P_0 = \frac{1}{2}\rho U_{ref}^3 \pi R^2$. Figure 6(b) confirms that the fraction of

available power barely increases with ST control, while it does with the helix control. It also shows, here again, that the CCW helix is more efficient than the CW one.

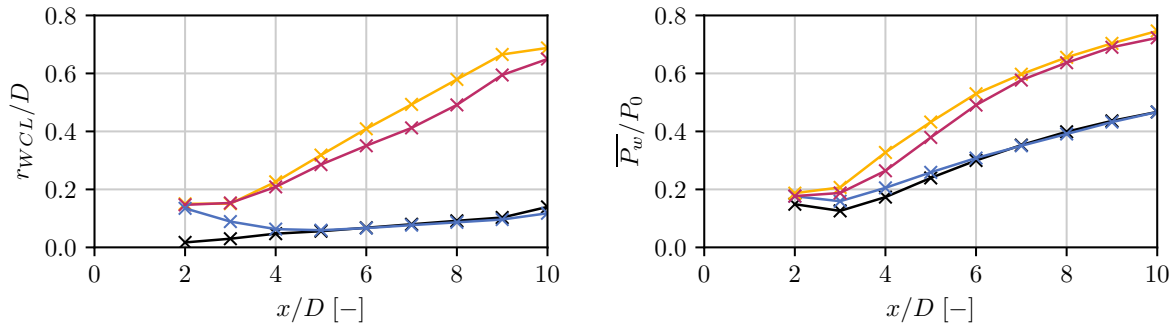

(a) WCL radial distance (b) Fraction of available power

Figure 6. Quantification of wake center line displacement (a) and power available in the wind for a downstream turbine (b) for BL (—), ST (—), CCW (—), CW (—).

4. Conclusions

This work relies on Large Eddy Simulations of the NREL 5MW to study IPC strategies aiming at wake mitigation and compares four cases: baseline, static IPC, CCW helix and CW helix. The two biggest outcomes from this study are that (i) dynamic set-points for the IPC controllers are needed to generate substantial lateral wake displacement and (ii) the rotating actuation of the helix interacts with the swirl, such that CCW and CW helix are not equivalent.

Results first show that the three IPC strategies create an imbalance in the rotor loading, hence displacing the application point of the thrust force from the rotor center. It is also highlighted that only a marginal in-plane force is generated with these strategies (1% of the thrust force). This questions whether this force should be considered as the sole driver of the phenomena further observed in the wake. In the very near wake ($x/D = 0$ to $x/D = 2$), the imbalance in the rotor loading results in the formation of in-plane vorticity, later being stretched into two lobes of streamwise vorticity (one positive, the other negative) in the inner wake. While in the ST case, these lobes do not persist further downstream, they are enhanced by dynamic actuation in the helix cases. In the CCW case, the wake swirl and the thrust motion rotate in the same direction. This eventually gives rise to a vortex system in the inner wake consisting in two negatively rotating vortices. In the CW case, the thrust force rotation acts against the swirl present in the wake. The vortex system in the inner wake consists in a positively rotating vortex and a negatively rotating one. These systems interact with the tip vortices to form, in the far wake, a system of counter-rotating vortices. In the CCW case, a CVP similar to that observed with yaw misaligned wakes rotates around the x-axis. In the CW case, a satellite zone of positive vorticity rotates around a dominant negative vortex. It is further shown, looking at the wake center line displacement and the power available in the wake, that the far-wake vortex system generated by the CCW helix is more efficient at both redirecting the wake and enhancing its mixing. Such coherent structures could not be observed in the far wake of the ST case. This shows that a static uneven load distribution cannot generate a wake deviation, conversely to an unsteady one, not too unlike what is observed in blooming jets [19] and in bio-locomotion [20].

A direct follow-up to this work would be to track the position and intensity of these dominant vortices and to understand how the near-wake vortex system evolves to become the one observed in the far wake. Investigating the interactions between the described vortex system in the near wake and the destabilization of the tip vortices could also be insightful. With this paper, we simplified the problem by considering uniform wind conditions with very low turbulence. Yet the

good performances of the helix have also been numerically demonstrated in the conventionally neutral atmospheric boundary layer in the work of Taschner et. al. [21]. Evaluating how the physics highlighted in this work translates to turbulent and sheared wind conditions is a key step towards understanding the full potential of the helix control.

Acknowledgements
This work is part of Hollandse Kust Noord wind farm innovation program where CrossWind C.V., Shell, Eneco, Grow and Siemens Gamesa are teaming up. Funding for the PhD's and PostDocs was provided by CrossWind C.V. and SiemensGamesa. The present research benefited from computational resources made available on Lucia, the Tier-1 supercomputer of the Walloon Region, infrastructure funded by the Walloon Region under the grant agreement n°1910247.

References

[1] J. Meyers, C. Bottasso, K. Dykes, P. Fleming, P. Gebraad, G. Giebel, T. Göçmen, and J.W. van Wingerden, "Wind farm flow control: prospects and challenges," *Wind Energy Science*, 2022.
[2] P. Fleming, P. Gebraad, S. Lee, J.W. van Wingerden, K. Johnson, M. Churchfield, J. Michalakes, P. Spalart, and P. Moriarty, "Evaluating techniques for redirecting turbine wakes using SOWFA," *Renewable Energy*, 2014.
[3] Siemens Gamesa, "Siemens gamesa now able to actively dictate wind flow at offshore wind locations." URL: `https://www.siemensgamesa.com/en-int/newsroom/2019/11/191126-siemens-gamesa-wake-adapt-en`, month = 11, year = 2010.
[4] M. Bastankhah and F. Porté-Agel, "Experimental and theoretical study of wind turbine wakes in yawed conditions," *Journal of Fluid Mechanics*, 2016.
[5] W. Munters and J. Meyers, "Dynamic strategies for yaw and induction control of wind farms based on large-eddy simulation and optimization," *Energies*, 2018.
[6] J. Frederik, B. Doekemeijer, S. Mulders, and J.W. van Wingerden, "The helix approach: Using dynamic individual pitch control to enhance wake mixing in wind farms," *Wind Energy*, 2020.
[7] H. Korb, H. Asmuth, and S. Ivanell, "The characteristics of helically deflected wind turbine wakes," *Journal of Fluid Mechanics*, 2023.
[8] M. Coquelet, M. Moens, M. Duponcheel, J.W. van Wingerden, L. Bricteux, and P. Chatelain, "Simulating the helix wake within an actuator disk framework: verification against discrete-blade type simulations," *Journal of Physics: Conference Series*, 2023.
[9] L. C. Cheung, K. A. Brown, D. R. Houck, and N. B. deVelder, "Fluid-dynamic mechanisms underlying wind turbine wake control with Strouhal-timed actuation," *Energies*, 2024.
[10] D. van der Hoek, B. V. den Abbeele, C. S. Ferreira, and J.W. van Wingerden, "Maximizing wind farm power output with the helix approach – experimental validation and wake analysis using tomographic PIV," *Wind Energy*, 2024.
[11] B. de Vos, B. Harder, T. Huisman, J. Gutknecht, and J.-W. van Wingerden, "Mimicking the helix with a porous disc for wind tunnel testing," *Journal of Physics: Conference Series*, 2024.
[12] J. Jonkman, S. Butterfield, W. Musial, and G. Scott, "Definition of a 5-MW reference wind turbine for offshore system development," *National Renewable Energy Lab*, 2009.
[13] E. Bossanyi, "Individual blade pitch control for load reduction," *Wind Energy*, 2003.
[14] D.-G. Caprace, P. Chatelain, and G. Winckelmans, "Lifting line with various mollifications: theory and application to an elliptical wing," *AIAA Journal*, 2019.
[15] D.-G. Caprace, G. Winckelmans, and P. Chatelain, "Assessment of the vortex particle-mesh method for efficient les of hovering rotors and their wakes," *AIAA Scitech 2021 Forum*, 2021.
[16] J. Mann, "Wind field simulation," *Probabilistic Engineering Mechanics*, 1998.
[17] J. Gutknecht, E. Taschner, A. Viré, and J.W. van Wingerden, "The physical mechanisms behind wake mixing enhancement with dynamic individual pitch control," in *NAWEA WindTech Conference*, 2023.
[18] N. Coudou, M. Moens, Y. Marichal, J. Van Beeck, L. Bricteux, and P. Chatelain, "Development of wake meandering detection algorithms and their application to large eddy simulations of an isolated wind turbine and a wind farm," *Journal of Physics: Conference Series*, 2018.
[19] T. B. Gohil, A. K. Saha, and K. Muralidhar, "Simulation of the blooming phenomenon in forced circular jets," *Journal of Fluid Mechanics*, 2015.
[20] M. Gazzola, P. Chatelain, W. M. Van Rees, and P. Koumoutsakos, "Simulations of single and multiple swimmers with non-divergence free deforming geometries," *Journal of Computational Physics*, 2011.
[21] E. Taschner, A. A. W. van Vondelen, R. Verzijlbergh, and J.W. van Wingerden, "On the performance of the helix wind farm control approach in the conventionally neutral atmospheric boundary layer," *Journal of Physics: Conference Series*, 2023.